JOURNAL OF AIRCRAFT
Vol. 47, No. 3, May–June 2010

Computational Investigation of Microscale Coaxial-Rotor Aerodynamics in Hover

Vinod K. Lakshminarayan* and James D. Baeder†
University of Maryland, College Park, MD 20742

DOI: 10.2514/1.46530

In this work, a compressible Reynolds-averaged Navier–Stokes solver is used to investigate the aerodynamics of a microscale coaxial-rotor configuration in hover, to evaluate the predictive capability of the computational approach and to characterize the unsteadiness in the aerodynamic flowfield of the microscale coaxial systems. The overall performance is well-predicted for a range of rpm and rotor spacing. As the rotor spacing increases, the top-rotor thrust increases and the bottom-rotor thrust decreases, while the total thrust remains fairly constant. The thrusts approach a constant value at very large rotor spacing. Top rotor contributes about 55% of the total thrust at smaller rotor spacing, which increases to about 58% at the largest rotor separation. The interaction between the rotor systems is seen to generate significant impulses in the instantaneous thrust and power. Unsteadiness is mainly caused due to blade loading and wake effect. Additional high-frequency unsteadiness was also seen due to shedding near the trailing edge. The phasing of the top vortex impingement upon the bottom rotor plays a significant role in the amount of unsteadiness for the bottom rotor. Interaction of the top-rotor tip vortex and inboard sheet with the bottom rotor results in a highly three-dimensional shedding on the upper surface of the blade in the outboard region and a two-dimensional shedding on the lower surface at the inboard portion of the blade. The wake of the top rotor contracts faster compared with that of the bottom rotor because of the vortex–vortex interaction. Further, the top-rotor wake convects vertically down at a faster rate due to increased inflow.

Nomenclature

c	=	Chord length of the airfoil, m
C_P	=	Power coefficient $= P/(\rho\pi R^2 U_{\text{tip}}^3)$ (referred to as C_Q)
C_p	=	Pressure coefficient
C_Q	=	Torque coefficient $= Q/(\rho\pi R^2 U_{\text{tip}}^2 R)$ (Equivalent to power coefficient, C_P)
$C_{Q_{\text{bot}}}$	=	Power coefficient of the bottom rotor
$C_{Q_{\text{ideal}}}$	=	Ideal power coefficient $= C_T^{3/2}/\sqrt{2}$
C_{Q_p}	=	Coefficient of power due to pressure forces
$C_{Q_{\text{top}}}$	=	Power coefficient of the top rotor
C_{Q_v}	=	Coefficient of power due to viscous forces
C_T	=	Thrust coefficient $=$ thrust$/(\rho\pi R^2 U_{\text{tip}}^2)$
$C_{T_{\text{bot}}}$	=	Thrust coefficient of the bottom rotor
$C_{T_{\text{top}}}$	=	Thrust coefficient of the top rotor
$C_{T_{\text{total}}}$	=	Total thrust coefficient of the coaxial system
$dC_{Q_{\text{rms}}}$	=	Root mean square fluctuation in power coefficient
$dC_{T_{\text{rms}}}$	=	Root mean square fluctuation in thrust coefficient
h	=	Distance between top and bottom rotor, m
q	=	Nondimensionalized second invariant of the velocity gradient tensor $\frac{\partial u_i}{\partial x_j}\frac{\partial u_j}{\partial x_i}$ (normalized by tip speed and blade chord)
R	=	Radius of the rotor, m
r	=	Radial location along the blade, m
Re	=	Reynolds number
U_{tip}	=	Tip speed, m/s
ρ	=	Density, kg/m^3
ψ	=	Wake age, deg
ψ_{b_1}	=	Wake age of top-rotor vortex, deg
ψ_{b_2}	=	Wake age of bottom-rotor vortex, deg

Presented as Paper 1069 at the 47th AIAA Aerospace Sciences Meeting and Exhibit, Orlando, Florida, 5–9 January 2009; received 28 July 2009; revision received 14 December 2009; accepted for publication 21 December 2009.

*Research Associate, Department of Aerospace Engineering; vinodkl@umd.edu.

†Associate Professor, Department of Aerospace Engineering; baeder@umd.edu. Associate Fellow AIAA.

Introduction

MICRO air vehicles (MAVs), as defined in the research program of Defense Advanced Research Projects Agency (DARPA), are cheap flying vehicles with no dimension exceeding 6 in. (15 cm), with a weight of no more than 100 g. There are three main types of MAV: fixed wing, flapping wing, and rotary wing. Even though fixed-wing MAVs are more efficient, they are not hover-capable and therefore cannot perform indoor missions effectively. Both flapping-wing and rotary-wing MAVs provide hover capability. Rotary-wing MAVs are more popular because of their simpler kinematics and therefore smaller mechanical losses compared with a flapping-wing design. However, rotary-wing vehicles are still not efficient enough to meet the objectives set by DARPA.

Coaxial rotor configuration is one of the technological solutions for increased helicopter forward speed, maneuverability, and load-carrying ability. With regard to MAVs, the most attractive feature of a coaxial design is the resulting compactness in the vehicle. Since two rotors produce the net thrust instead of a single rotor in the conventional design, the diameter of the rotors can be reduced to carry the same amount of weight. Secondly, eliminating the tail rotor and tail boom results in a smaller and lighter vehicle.

However, in a coaxial-rotor configuration, the two rotors and their wakes interact with each other, producing a more complicated flowfield than is found in a single rotor system. A major portion of the lower rotor continually operates in the wake system of the upper rotor. This has a significant effect on the inflow distribution of the overall system, and also on the boundary layer of the lower rotor blades. This interacting flow can, in general, result in a loss of net rotor-system aerodynamic efficiency. Additionally, this can result in an undesired unsteadiness in the flowfield even under hovering conditions.

Aerodynamics and flow physics of either microscale single rotor or full-scale coaxial rotor are relatively less studied and understood. With the growing desire for efficient rotary-wing MAVs, which typically operate between $Re = 10^3$–10^5, accurate predictions of low-Mach, viscous-dominated flows are in increasing demand. Because of the difficulties involved in experimentally studying MAVs and the breakdown of analytical correlations for drag and boundary-layer behavior for this Reynolds-number range, accurate

computational results are of critical importance to MAV research. Recently, the current authors have investigated microscale single-rotor [1] and full-scale coaxial-rotor [2] aerodynamics in a very detailed manner. A brief summary of some of the results and experimental validation from the earlier studies are provided in this paper. The goal of this work is to combine these methodologies and extend the use of a compressible Reynolds-averaged Navier–Stokes (RANS) solver to study the performance and flow physics of a microscale coaxial rotor. This will help in determining the feasibility of using a coaxial configuration for a rotary MAV.

There are certain challenges involved in this study. Unlike in fixed-wing vehicles or even rotary-wing vehicles in forward flight, the flowfield of hovering rotors is significantly influenced by the trailed wake system since it remains in the proximity of the rotor at all times. Additionally, the effect of the wake is highly significant since one is interested in its interaction with the rotor blades. Therefore, an accurate representation of the tip-vortex formation and evolution is essential in achieving high-fidelity performance predictions of hovering MAVs. Hence, accurate numerical schemes and reliable turbulence models need to be used and the resulting methodology needs to be carefully validated with experiments if the computational fluid dynamics (CFD) results are to be considered reliable.

Methodology

The computations are performed using the overset structured mesh solver OVERTURNS [3]. To allow for adequate mesh resolution and ease of grid generation, structured overset meshes are used. All the computations are performed in a time-accurate manner in the inertial frame of reference. Time integration is performed using the second-order implicit backwards difference method scheme with either the lower–upper symmetric Gauss–Siedel method [4] or the diagonal form of implicit approximate factorization method developed by Pulliam and Chaussee [5] for inversion. When low Mach numbers are involved, time-accurate low-Mach preconditioning in a dual-time scheme described by Buelow et al. [6] and Pandya et al. [7] is used. The low-Mach preconditioning is based on the one developed by Turkel [8]. The preconditioning is used not only to improve convergence but also to improve the accuracy. The inviscid terms are computed using a third-order MUSCL scheme using Koren's limiter with Roe's flux difference splitting, and the viscous terms are computed using second-order central differencing. The Spalart–Allmaras [9] turbulence model is employed for the RANS closure. This one-equation model has the advantages of ease of implementation, computational efficiency, and numerical stability. The production term in this eddy-viscosity model is modified [10] to account for the reduction of turbulence in the vortex core due to flow rotation effects. The downwash velocity in the bottom plane below the rotor can be significant. To account for this and to properly represent the inflow at the other far-field boundaries, the point-sink boundary-condition approach of Srinivasan and Baeder [11] is used. Implicit hole-cutting technique [12] is used to find the connectivity information between various overset meshes.

Microscale Single-Rotor Validation

Hovering microscale single-rotor validation is done by exploring the experimental results obtained by Ramasamy et al. [13,14] on a two-bladed hovering rotor at a tip Reynolds number of 32,400, tip Mach number of 0.08, and a wing aspect ratio of 4.39. The resulting solidity is 0.145. The untwisted rectangular blades used a 3.3% curvature circular-arc airfoil with a thickness of 3.7%. The baseline section has a blunt leading as well as trailing edge (BLTE). Experiments were also performed on sections that were slightly different from the baseline section. One of them is the baseline section with sharpened leading and trailing edge (SLTE). Performance data is available at various collective angles. High-resolution flow visualization and particle-image-velocimetry flowfield data is available for the case with collective angle of 12° using the baseline sectional profile.

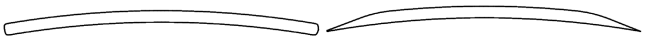

a) Blunt leading and trailing edge (BLTE) **b) Sharp leading and trailing edge (SLTE)**

Fig. 1 Computational sectional profiles for microscale single rotor.

Computations are performed on rotor blades with sectional profiles shown in Fig. 1. The modeled geometries are mostly similar to the corresponding experimental geometries. Minor modifications are made to the geometries to allow simulation using *C*-type grid. The geometry with sharp leading edge is modeled using a slightly rounded leading edge, and the geometry with blunt trailing edge is modeled with marginally smoothened trailing edge. It should be noted that the differences in the modeled geometry is so small that it is not expected to have any significant influence on the solution.

A two-mesh overset system with a body-conforming blade mesh and a cylindrical background mesh is used for the computations. Information is exchanged from one grid to the other by means of linear interpolation. For 12° collective setting cases, where the flowfield is compared with the experiments, computations are performed on a fine mesh with the blade mesh having $267 \times 185 \times 99$ points in the streamwise, spanwise, and normal directions, respectively, and the background cylindrical mesh having $127 \times 186 \times 198$ points in the azimuthal, radial, and vertical directions, respectively. In the most refined regions, the background mesh has a grid spacing of 0.02 chords in both the radial and the vertical directions. Along the azimuthal direction, a grid plane is spaced every 1.5°. For all other collective settings, where only performance data is compared, computations are performed on a coarser mesh obtained by leaving out every other point in the spanwise and normal direction. The chosen time-step size corresponds to 0.125° of azimuth for the fine-mesh and 0.25° of azimuth for the coarse-mesh calculations. Some sample performance comparisons and flowfield visualizations are shown to provide confidence in the ability to predict rotor flows at the microscale; more details are provided in earlier work [1].

Performance Comparison

Figure 2 compares the computed performance with the experimentally measured values [14]. It can be seen that the computed performance for both BLTE and SLTE geometries show good agreement with the experimental results. At higher thrust levels, the power is underpredicted by about 4–5% for the SLTE geometry and overpredicted by 1–2% for the BLTE geometry. However, the overall comparison between the computational and the experimental result is reasonably good and therefore demonstrates the capability of the current computational study to provide good performance predictions. It should be noted that the performance results obtained using the fine mesh for the 12° collective setting are comparable to

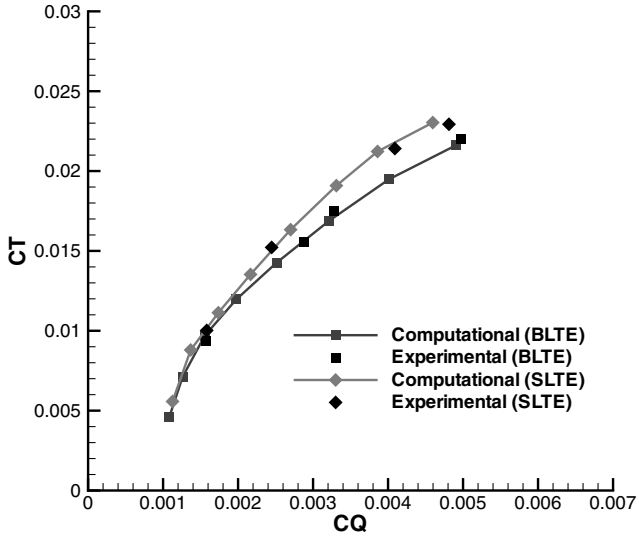

Fig. 2 Performance comparison (C_T vs C_Q) with experimental data [14] for microscale single rotor.

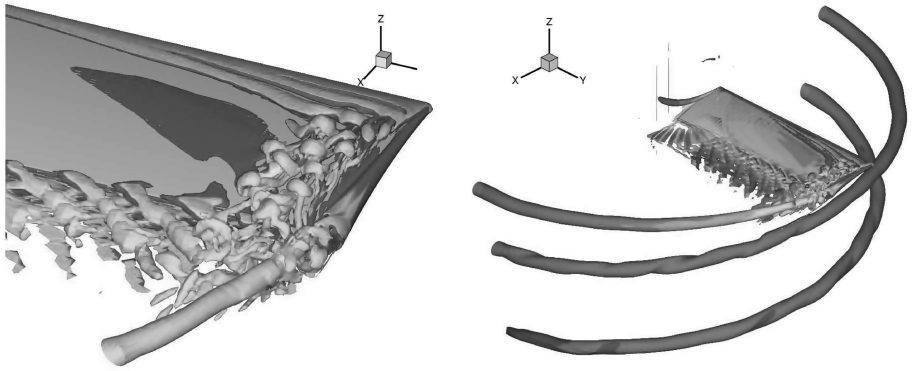

a) $q = 8.0$ b) $q = 0.5$

Fig. 3 Isosurfaces of second invariant of the velocity gradient tensor at 12° collective setting for microscale single rotor, BLTE geometry.

the coarse-mesh results and, therefore, show grid convergence in the performance data.

Flowfield Visualizations

Next, qualitative features in the flowfield are examined. Figure 3a shows isosurfaces of the so-called q criterion [15] shaded with vorticity magnitude contour near the blade surface for 12° collective setting for BLTE geometry. It is evident that the tip-vortex flowfield is extremely complicated because of the presence of a variety of secondary structures near the blade tip. Within a short distance downstream of the trailing edge, these structures appear to have merged with the tip vortex.

Figure 3b shows the isosurface of q-criterion (shaded with vorticity magnitude contour) in the entire flowfield for the BLTE geometry at 12° collective setting. The resolution of the tip vortex for three blade passages is clearly evident. Beyond this wake age, the background mesh becomes too coarse to accurately represent the details of the tip vortex. An interesting feature revealed from this figure is the fact that while the tip vortex is smooth initially, it seems to get twisted near the first blade passage. This is because of the fact that it is embedded in a highly strained field due to the presence of the evolving tip vortex (note that the vertical convection of the tip vortex is relatively low before the first pass as has been well-documented [16,17]) and other near-blade structures. It is also seen that after the first pass, the vortex becomes wavy along its axis, thus suggesting slight instability. Interestingly, such an instability was observed experimentally even for a full-scale rotor [16].

Full-Scale Coaxial-Rotor Validation

The hovering coaxial experimental setup of Harrington's rotor 2 [18] is used to validate the computational predictions for the coaxial rotors at full scale. It consists of two two-bladed rotors arranged to form a coaxial system. The aspect ratio of the blade is 8.33, resulting in an individual rotor solidity of 0.076. The interrotor spacing is 1.33 chords ($h/R = 0.16$). The blade uses a NACA airfoil with a linearly varying thickness of 27.5% at $0.2R$ to 15% at R. The tip Reynolds number is 3.5×10^6 and the tip Mach number is 0.352.

A six-mesh system consisting of two blade meshes, two nested background meshes, and two cylindrical outer background meshes is used. The blade mesh, the nested background mesh, and the outer background mesh of each rotor form an overset system. Nested background meshes are used to smoothly transfer the solution from the blade mesh to the outer background mesh. The outer background meshes communicate with each other by means of a sliding mesh interface. The solution is transferred from one mesh to the other by using a third-order slope limited M3-quartic interpolation of Huynh [19]. Periodicity is assumed such that only one blade from each rotor system is actually simulated.

All the computations are performed on top- and bottom-rotor blade meshes having $267 \times 155 \times 111$ points in the streamwise, spanwise, and normal directions, respectively; the nested background meshes have $97 \times 204 \times 72$ points, the top-rotor outer background mesh has $97 \times 270 \times 61$ points, and the bottom-rotor outer background mesh has $97 \times 270 \times 180$ points in the azimuthal, radial, and vertical directions, respectively. The total number of mesh points used is 18.3 million. The blade mesh of the top rotor is sufficiently fine in the tip region to resolve the tip-vortex formation.

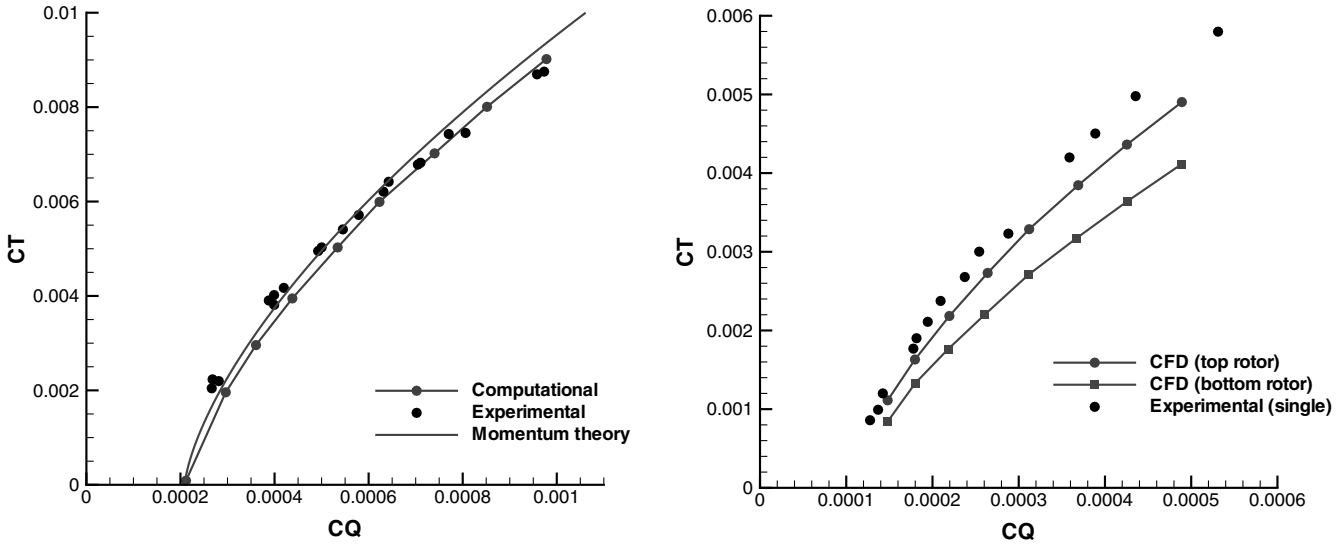

a) Total C_T (mean) vs total C_Q (mean) b) C_T (mean) vs C_Q (mean) for individual rotors

Fig. 4 Comparison of performance with experimental data [18] for full-scale coaxial rotor.

For the bottom rotor, the grid is redistributed such that the inboard region is highly refined as well, to resolve the wake interaction. In the most refined regions, the nested background mesh has a grid spacing of 0.0165 chords in the vertical direction, while the outer background mesh has a grid spacing of 0.033 chords in the same direction. In the radial direction, both the nested and outer background meshes have grid spacing of 0.02 chords in the most refined region. Along the azimuthal direction, a grid plane is spaced every 2° in the outer background mesh. For the nested background mesh, the azimuthal spacing varies from 0.3° near the blade to 2° in its outer boundaries. The chosen time-step size corresponds to 0.125° of azimuth. Some sample performance comparisons (mean total) and predicted unsteady performance time histories are shown to provide confidence in the ability to predict coaxial-rotor flows at the full scale; more details are provided in earlier work [2].

Mean Performance

Figure 4a compares the computed variation of mean total thrust coefficient with mean total power coefficient with the measured values. The total performance is well-predicted. At lower collectives, the power is slightly overpredicted for a given thrust, whereas at higher collectives the power is marginally underpredicted for a given thrust level. Plotted along with the experimental data and the CFD results is the curve fit using momentum theory for coaxial rotor [20]. The results using momentum theory also show similar trend as the CFD results.

Figure 4b shows the mean performances of the individual rotors (zero collective case is excluded). As expected, for the bottom rotor, the performance degrades significantly (about 40% increase in power at same thrust at higher thrust levels) compared with that of a single rotor because of the influence of the wake from the top rotor. It is interesting to note that even the performance of the top rotor is slightly degraded (about 15% increase in power at same thrust at higher thrust levels), indicating that the bottom rotor has some influence on the flowfield of the top rotor. Similar observations were made by Nagashima and Nakanishi [21] in their experimental results and by Syal [22] for Harrington's rotor 1 using a free vortex method.

Unsteady Performance

Figure 5 shows the temporal variation of C_T and C_Q over one revolution for various thrust levels. Note that, when viewed from above, the top rotor rotates in an anticlockwise fashion and the bottom rotor rotates clockwise. Therefore, the azimuthal locations of the top and bottom rotors are measured in their respective directions

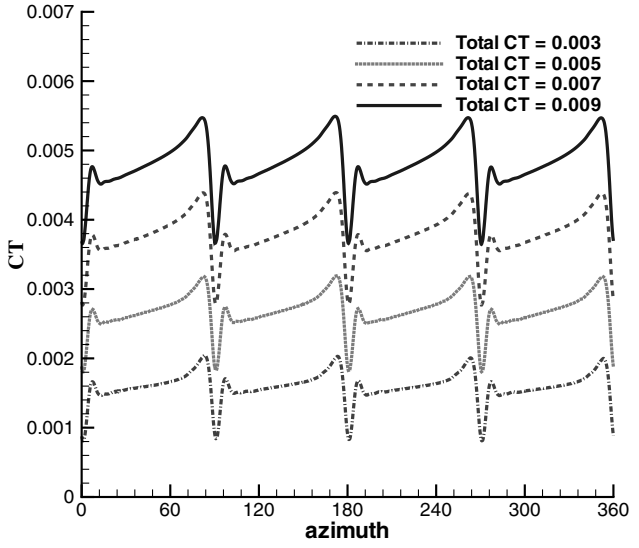

a) Top-rotor C_T variation

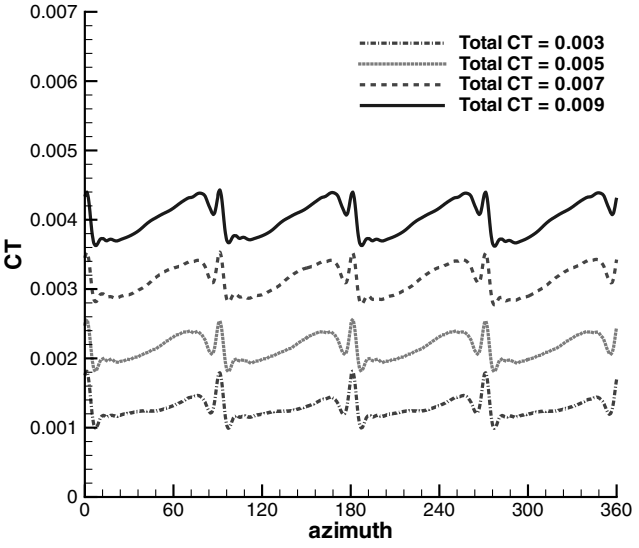

b) Bottom-rotor C_T variation

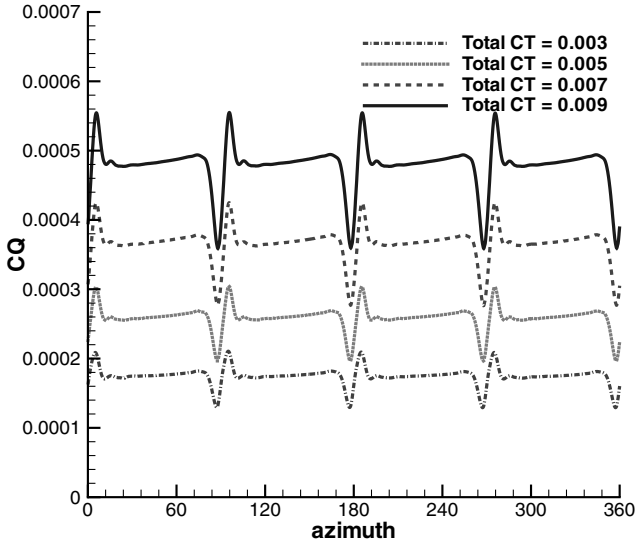

c) Top-rotor C_Q variation

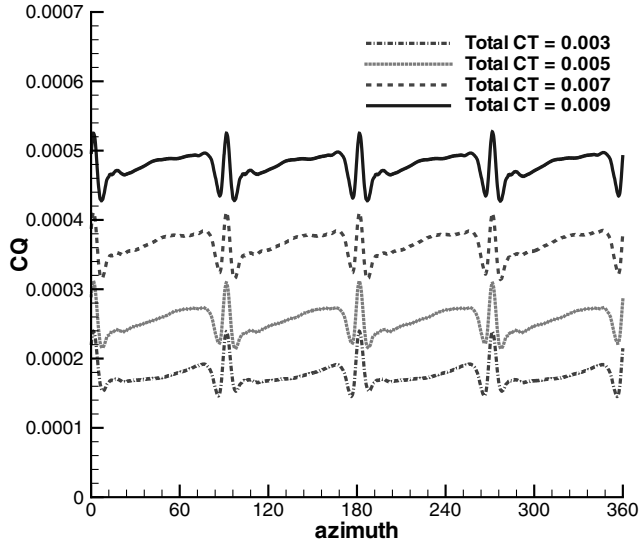

d) Bottom-rotor C_Q variation

Fig. 5 Temporal variation of C_T and C_Q of the top and bottom rotors over one revolution for various thrust levels for full-scale coaxial system.

of rotation. From the figure, the unsteadiness is clearly seen with a dominant 4/rev frequency (number of times a blade of one rotor encounters a blade of the other rotor in one revolution). A higher frequency variation can be seen in the form of spikes when the blades are very close to each other. Such a variation can be attributed to the venturi effect caused by the thickness of the blades, which leads to a reduction in pressure between the rotors. As a result, the thrust of the top rotor spikes down whereas the thrust of the bottom rotor spikes up. Apart from the thickness effect, there is also a loading effect created by the bound circulation of the blades. As the blades of the top and bottom rotors approach each other, each blade induces an upwash on the other blade. The upwash increases as the blades approach each other, but after a certain point it starts decreasing, changes sign, and acts as a downwash. The strength of the downwash is seen to initially increase and then starts decreasing as the blades move away from each other. Correspondingly, the forces on both the top and the bottom rotor increase as the blades approach, then decrease, and then increase again as they move away. Furthermore, while the thrust and the power of the top rotor show an impulsive but phased behavior, the features are more spread out and distinct for the bottom rotor, which lies in the wake of the top rotor.

Microscale Coaxial-Rotor Validation

With validation of the predictive capability of OVERTURNS for microscale single-rotor and full-scale coaxial rotor in hover established, the extension is made to the microscale coaxial-rotor case by exploring the experimental results obtained by Bohorquez [23] on a hovering coaxial system having two two-bladed rotors. The aspect ratio of the blade is 4.98, resulting in an individual rotor solidity of 0.128. The blades have untwisted planform, which uses circular-arc airfoil with sharpened leading and trailing edges. The airfoil has a camber of 6% and a thickness of 2.2%. The experiment was conducted at different rotor rpm and interrotor spacing. The collectives of both the top and bottom rotors are set at 16°.

The mesh system used for the computation is similar to that used for the full-scale coaxial-rotor calculation. A six-mesh system consisting of two blade meshes, two nested background meshes, and two cylindrical outer background meshes is used. Computations are performed on top- and bottom-rotor blade meshes having $267 \times 93 \times 50$ points in the streamwise, spanwise, and normal directions, respectively; the nested background meshes have $97 \times 124 \times 56$ points, the top-rotor outer background mesh has $97 \times 149 \times 49$ points, and the bottom-rotor outer background mesh has $97 \times 149 \times 143$ points in the azimuthal, radial, and vertical directions, respectively. The total number of mesh points used is 6.6 million. Further refinement of the meshes did not show much change in the solution. A smaller number of mesh points can be used for the microscale rotor due to the lower aspect ratio and the relatively larger expected sizes of the boundary layers and the core of the vortices. Figure 6 shows the blade and background meshes. In the most refined regions, the nested background mesh has a grid spacing of 0.02 chords in the vertical direction, while the outer background mesh has a grid spacing of 0.04 chords in the same direction. In the radial

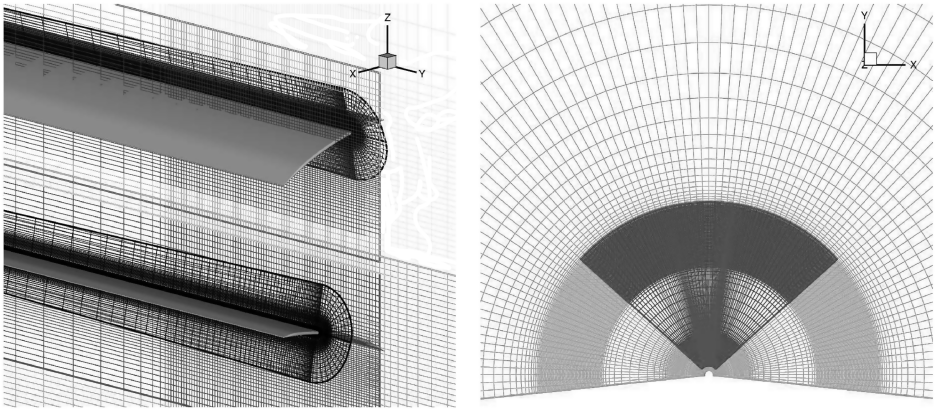

a) Blade meshes along with cylindrical meshes b) Inner and outer cylindrical meshes

Fig. 6 Computational mesh for microscale coaxial-rotor system.

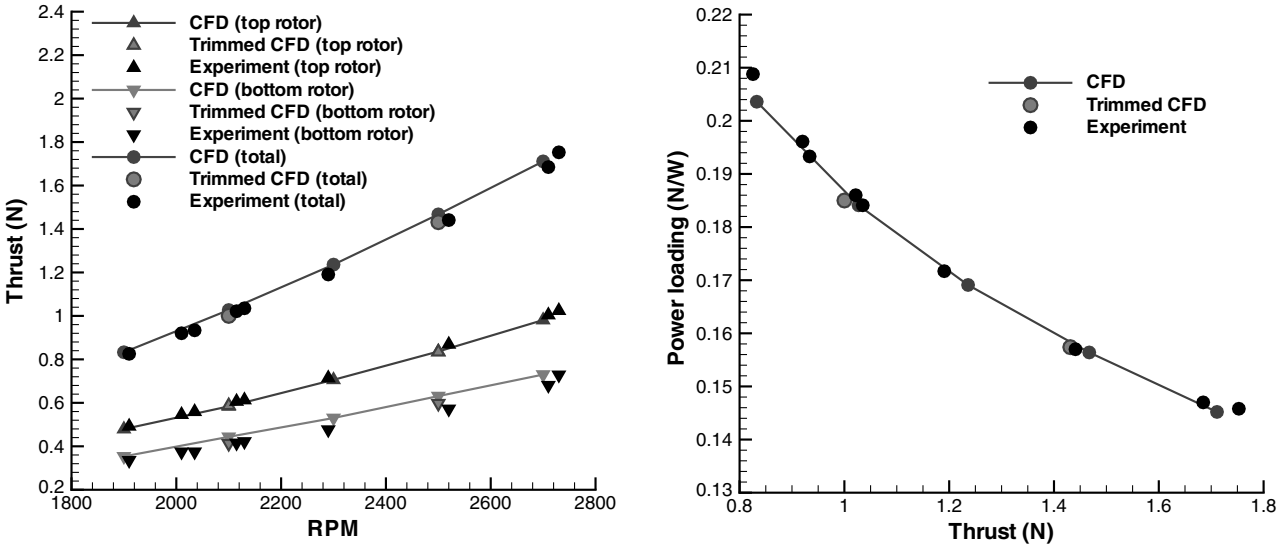

a) Thrust (mean) vs RPM b) Power loading (mean) vs thrust (mean)

Fig. 7 Performance comparison with experimental data [23] at different rpm for microscale coaxial rotor.

direction, both the nested and outer background meshes have grid spacing of 0.025 chords in the most refined region. Along the azimuthal direction, a grid plane is spaced every 2° in the outer background mesh. For the nested background mesh, the azimuthal spacing varies from 0.3° near the blade to 2° in its outer boundaries. The outer boundary of the background mesh extends to $3R$ above the top rotor, $4.5R$ below the bottom rotor, and $4R$ from the tip of the blade. The chosen time-step size corresponds to 0.125° of azimuth.

Effect of RPM

Experiments were conducted for a range of rpm varying from 1900 to 2700. Correspondingly, the tip Reynolds number varied from 19,000 to 27,000 and the tip Mach number ranged from 0.0665 to 0.0945. For the rpm sweep, the rotor spacing is fixed at $h/R = 0.446$. Figure 7a shows the comparison between the computed and the measured variation of mean thrust with rpm for individual rotors as well as the entire system.

In the experimental test, the top and bottom rotors were torque-balanced by changing the rpm of the bottom rotor, while keeping the top-rotor rpm fixed. However, it was found that the percentile difference in rotational speed required for torque balance is less than 2%. Therefore, it should be reasonable to approximate the rotational speed of the bottom rotor to be the same as that of the top rotor. To verify this, two sets of computations are performed: one set that assumes identical top- and bottom-rotor rotational speeds and the other set that is torque trimmed by using different rotational speed for the bottom rotor.

For the calculations assuming identical rotational speed for the top and bottom rotors, the total system thrust is seen to be well-predicted (within 3%) at all rotational speeds. Top-rotor thrust is under-predicted by approximately <2% at all speeds whereas the bottom-rotor thrust is overpredicted by approximately <8%. A better thrust prediction is obtained using the torque-trimmed calculations. The overprediction in the bottom-rotor thrust reduces to within 3% and that of the entire system reduces to within 1%. However, the improvement in prediction capability is marginal compared with the increase in computational cost required for torque trimming. Consequently, all the computations in the following sections are performed assuming identical top- and bottom-rotor rotational speed.

Figure 7b shows the comparison of mean power loading [thrust (N) / power (W)] vs mean thrust for the total system. Clearly, the power is very well-predicted for both sets of computation.

Table 1 Computed mean torque coefficient for microscale coaxial system

h/R	$C_{Q_{\text{top}}}$	$C_{Q_{\text{bot}}}$	$C_{Q_{\text{total}}}$	$\lvert C_{Q_{\text{top}}} - C_{Q_{\text{bot}}} \rvert$
0.268	0.00384	0.00422	0.00806	0.00038
0.357	0.00387	0.00410	0.00797	0.00023
0.446	0.00388	0.00407	0.00795	0.00019
0.536	0.00389	0.00407	0.00796	0.00018
0.625	0.00392	0.00408	0.00800	0.00016

Table 2 Computed mean thrust coefficient for microscale coaxial system

h/R	$C_{T_{\text{top}}}$	$C_{T_{\text{bot}}}$	$C_{T_{\text{total}}}$	$C_{T_{\text{top}}}/C_{T_{\text{total}}}$	$C_{T_{\text{total}}}$ (Expt. [23])
0.268	0.0199	0.0163	0.0362	0.55	0.0349
0.357	0.0205	0.0158	0.0363	0.56	0.0349
0.446	0.0208	0.0157	0.0365	0.57	0.0350
0.536	0.0210	0.0155	0.0365	0.58	0.0350
0.625	0.0212	0.0153	0.0365	0.58	0.0350

Effect of Rotor Spacing

Five different rotor spacings given by $h/R = 0.268, 0.357, 0.446, 0.536$, and 0.625 are studied. The rpm for this study is fixed at 2000. Correspondingly, the tip Reynolds number is 20,000 and tip Mach number is 0.07.

Mean Performance

Table 1 summarizes the mean values of power (C_Q) coefficient obtained from CFD for individual rotors as well as for the entire system for all the rotor spacings. It can be seen that for all cases, torque is trimmed to within 5% error, showing that it is reasonable to assume identical rotational speed for the top and bottom rotors. Table 2 summarizes the mean values of thrust (C_T) coefficient obtained from CFD for individual rotors as well as for the entire system. Also shown is the total thrust obtained from the experiments. It can be seen that the computed top- and bottom-rotor thrusts show opposite trends as the rotor spacing increases. While the top-rotor thrust increases with the rotor spacing, the bottom-rotor thrust decreases as the rotor separation increases. Both the rotor thrusts approach a constant value at very large rotor spacing. Because of the opposing trends in the top- and bottom-rotor thrusts, the total thrust of the system is seen to remain fairly constant with the rotor spacing, apart from the marginal increase in value at smaller rotor-separation distances. Similar trend can be seen even in the experimental results. Table 2 also shows the ratio of the top-rotor thrust to the total thrust. Top rotor contributes to about 55% of the total value at smaller rotor spacing and increases to about 58% at the largest rotor separation. It should be mentioned here that full-scale coaxial rotor also showed similar thrust sharing [2].

Table 3 Computed RMS fluctuation of power (torque) coefficient for microscale coaxial system

h/R	$dC_{Q_{\text{rms}}}$ (top rotor)	% fluctuation	$dC_{Q_{\text{rms}}}$ (bottom rotor)	% fluctuation	$dC_{Q_{\text{rms}}}$ (total)	% fluctuation
0.268	0.000141	3.67%	0.000626	14.83%	0.000628	7.79%
0.357	0.000094	2.43%	0.000304	7.41%	0.000234	2.93%
0.446	0.000053	1.37%	0.000168	4.13%	0.000204	2.57%
0.536	0.000048	1.23%	0.000357	8.77%	0.000376	4.71%
0.625	0.000039	0.99%	0.000405	9.93%	0.000405	5.06%

Table 4 Computed RMS fluctuation of thrust coefficient for microscale coaxial system

h/R	$dC_{T_{\text{rms}}}$ (top rotor)	% fluctuation	$dC_{T_{\text{rms}}}$ (bottom rotor)	% fluctuation	$dC_{T_{\text{rms}}}$ (total)	% fluctuation
0.268	0.00105	5.28%	0.00164	10.06%	0.00237	6.55%
0.357	0.00065	3.17%	0.00074	4.68%	0.00074	2.04%
0.446	0.00040	1.92%	0.00057	3.63%	0.00088	2.41%
0.536	0.00036	1.71%	0.00091	5.87%	0.00120	3.29%
0.625	0.00024	1.13%	0.00105	6.86%	0.00117	3.21%

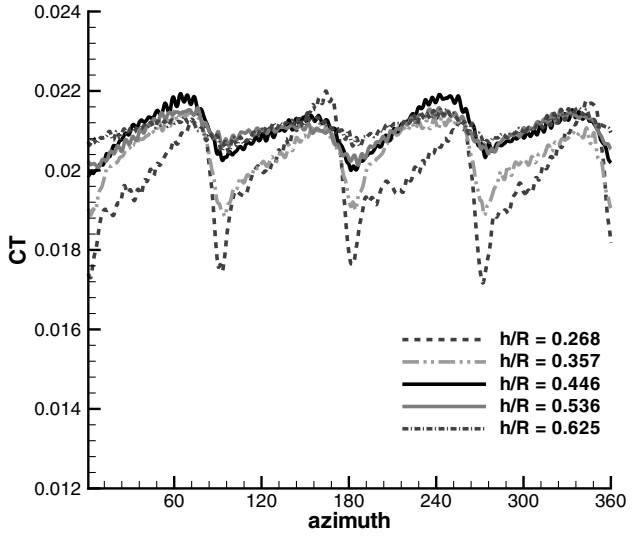

a) Top-rotor C_T variaton

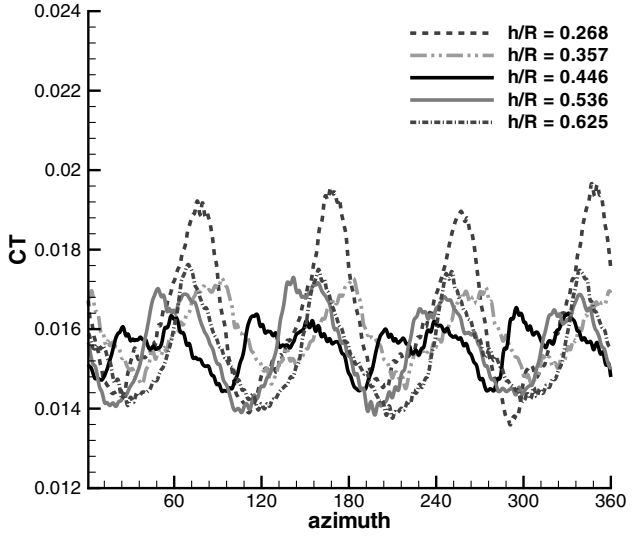

b) Bottom-rotor C_T variation

Fig. 8 Temporal variation of C_T of the top and bottom rotors over one revolution for various rotor spacing for microscale coaxial system.

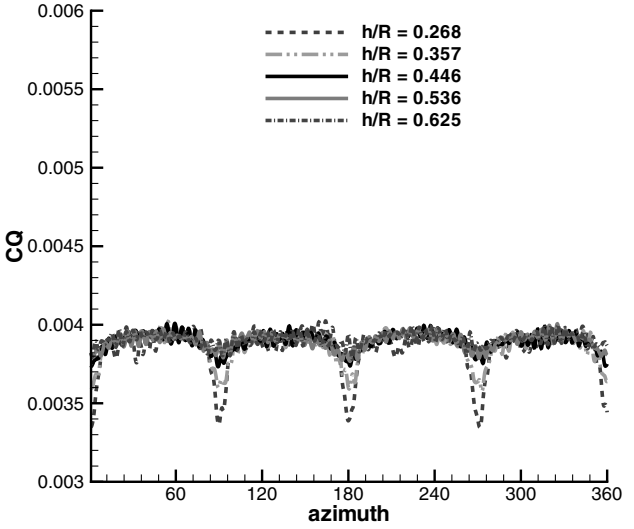

a) Top-rotor C_Q variation

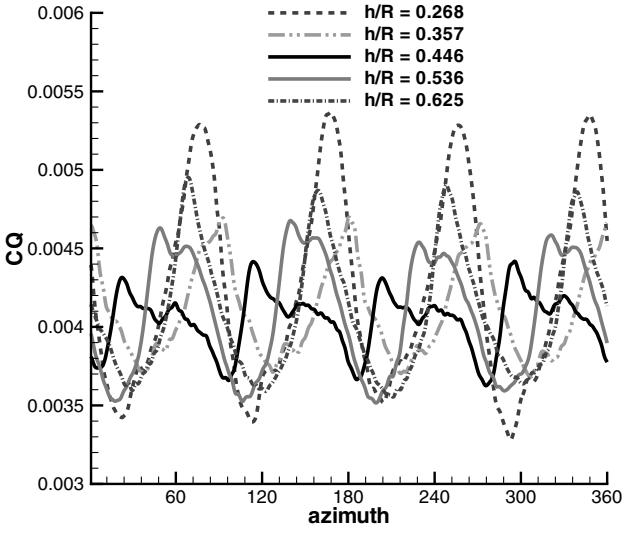

b) Bottom-rotor C_Q variation

Fig. 9 Temporal variation of C_Q of the top and bottom rotors over one revolution for various rotor spacing for microscale coaxial system.

Unsteady Performance

A measure of the unsteadiness in thrust and power is the root mean square (RMS) value of the temporal variations, and this is summarized in Tables 3 and 4. For the top rotor, the absolute value of the fluctuation decreases with increasing rotor spacing; however, surprisingly, for the bottom rotor, the absolute fluctuations initially decrease and then increase again as the rotor separation increases. The reason for this will be discussed later in the section. The fluctuations of the integrated quantities of the whole system follow similar trend as that of the bottom rotor. In general, there is 3–8% fluctuation in all integrated quantities, which could be significant for vibration and acoustic characteristics. Note that experiments typically provide only the mean performance data; obtaining the unsteady data is very challenging.

Figures 8 and 9, respectively, show the temporal variation of C_T and C_Q over one revolution for all rotor spacings. As seen for the full-scale coaxial rotor, the figure clearly shows the unsteadiness with a dominant 4/rev frequency. A high-frequency noiselike variation is seen at all times due to shedding near the trailing edge, which was seen even for the microscale single rotor (Fig. 3). This variation is more obvious in the top-rotor forces. The higher-frequency variation seen in the full-scale coaxial rotor near the blade passage due to thickness effect is not very prominent. This is because the airfoil sections used in the blades here are relatively thin and therefore do not produce a significant thickness effect. The loading effect is seen to be present, which decreases with the rotor spacing, similar to the full-scale coaxial rotor. This is particularly clear from the temporal variation of the integrated quantities of the top rotor, for which the unsteadiness decreases with the increasing rotor separation.

However, for the bottom rotor, the unsteadiness is not seen to follow any particular trend as the rotor spacing increases. This is in contrast to the full-scale system [2], for which the unsteadiness in the bottom-rotor forces also decreases with the rotor spacing. The reason for the differences can be understood by comparing the temporal variation of thrust and power for the bottom rotor of the microscale system (Figs. 8b and 9b) along with that of the full-scale system (Figs. 5b and 5d). All the plots show two peaks (apart from the peak due to thickness effect on the full-scale system), which recurs every 90° azimuth. The peak which occurs close to the blade passage is due to the loading effect, and the other peak occurs when the vortex from the top rotor impinges upon the bottom rotor (for some of the plots, the peaks coincide). Clearly, as opposed to the full-scale system, the peak due to vortex impingement is more prominent and at times larger than the peak due to loading effect for the microscale rotor. This suggests

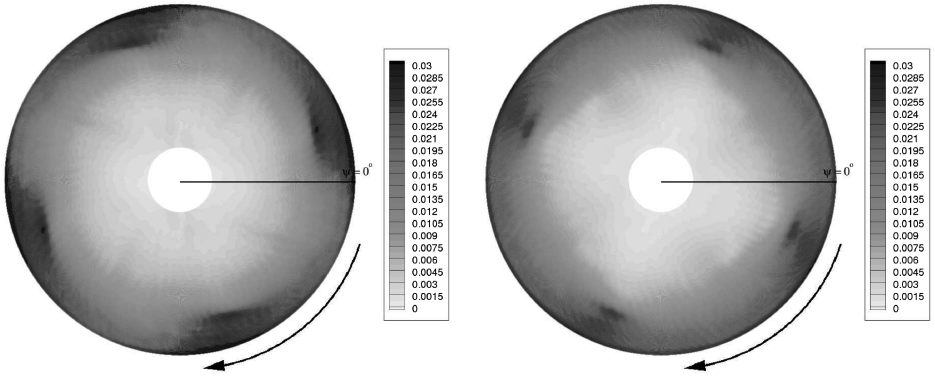

a) h/R = 0.268 b) h/R = 0.446

Fig. 10 Sectional thrust ($R\frac{dC_T}{dr}$) contour for the bottom rotor of microscale coaxial system.

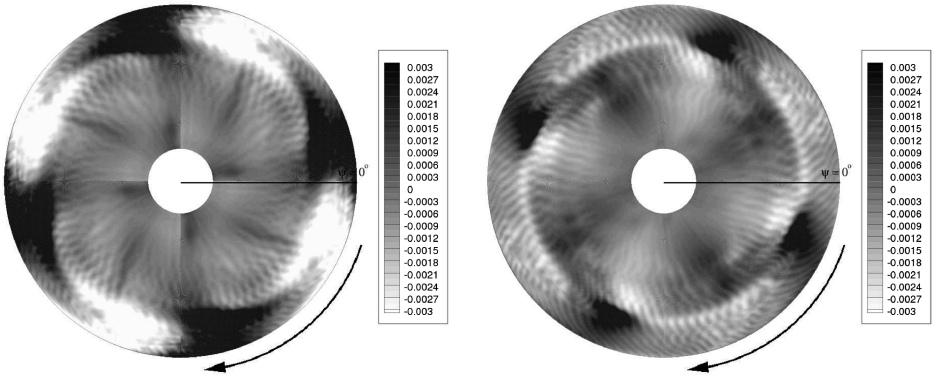

a) h/R = 0.268 b) h/R = 0.446

Fig. 11 Fluctuation in sectional thrust ($R\frac{dC_T}{dr}$) contour for the bottom rotor of microscale coaxial system.

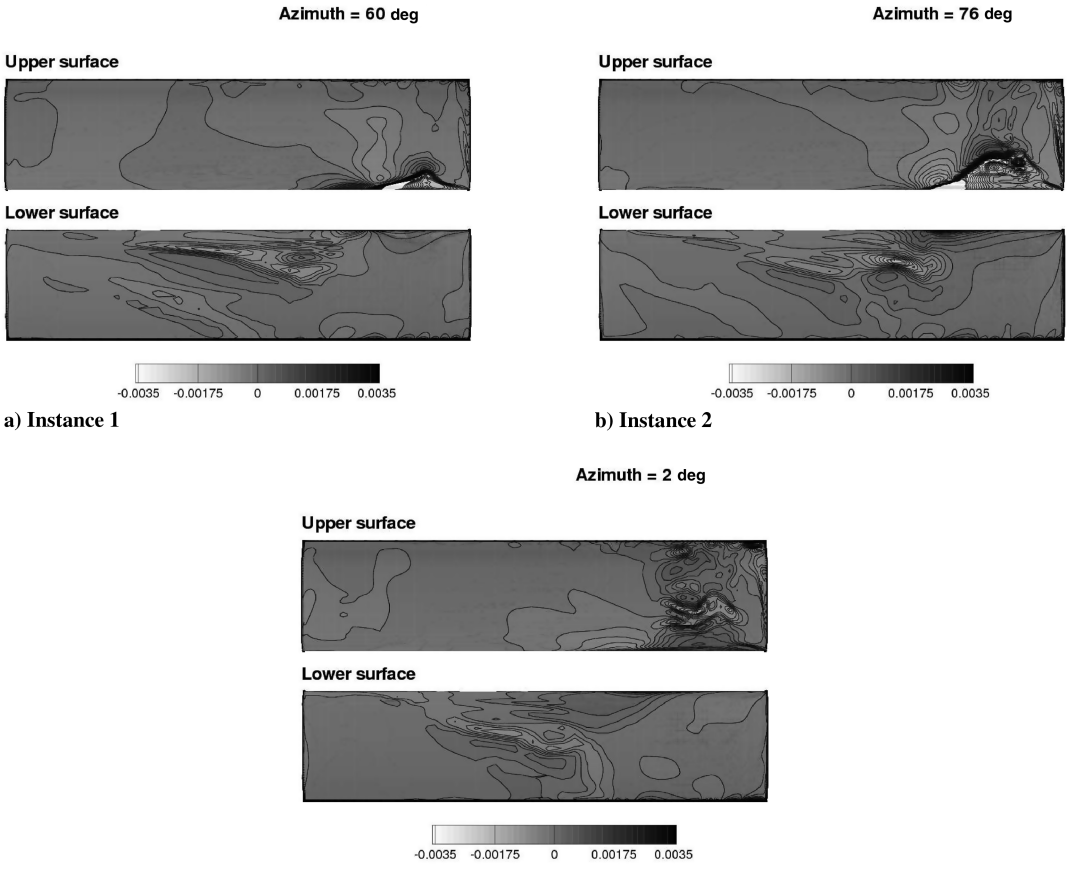

a) Instance 1 b) Instance 2

c) Instance 3

Fig. 12 Fluctuation in the surface pressure for the $h/R = 0.268$ case of microscale coaxial system.

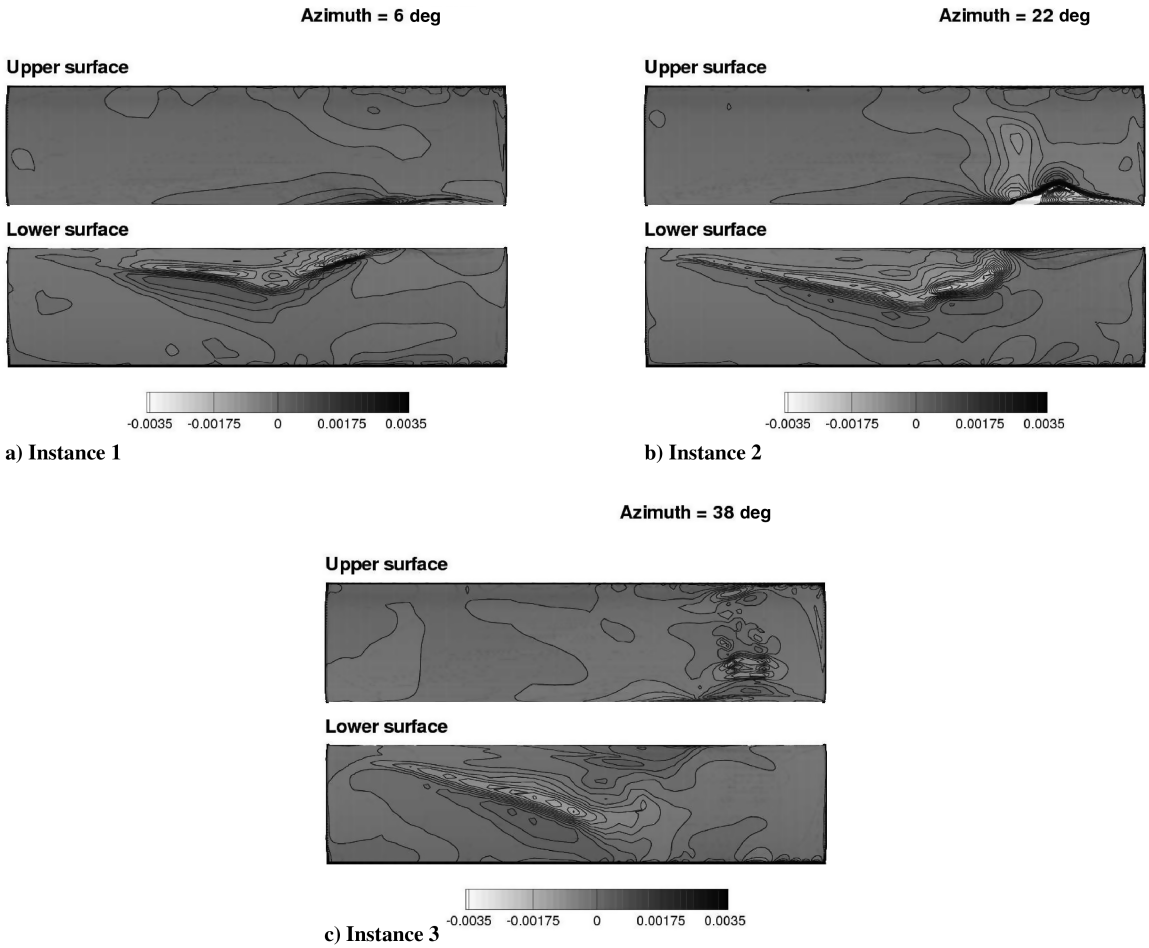

Fig. 13 Fluctuation in the surface pressure for the $h/R = 0.446$ case of microscale coaxial system.

that, contrary to the full-scale system, the wake effect for the microscale system is comparable or maybe even predominant over the loading effect when the rotor spacing is large. Therefore, the unsteadiness in the integrated quantities for the bottom rotor of the microscale coaxial system need not necessarily decrease as the rotor spacing increases. On the other hand, because of the decrease in the dominant loading effect for the full-scale systems, increase in rotor spacing almost always results in a decrease in the unsteadiness of the bottom-rotor forces. In Fig. 8, the peak due to vortex impingement is seen to move to a later azimuth as the rotor spacing increases, as it takes longer to convect down vertically. The peak due to vortex impingement for $h/R = 0.268$, 0.357, 0.446, 0.536, and 0.625, respectively, occurs at 76, 2, 22, 48, and 68° azimuth location, which recurs at 90° azimuth. For $h/R = 0.268$ and $h/R = 0.625$, the peaks due to vortex impingement and the loading effect are almost coincident, whereas for $h/R = 0.446$, the peaks are farthest apart.

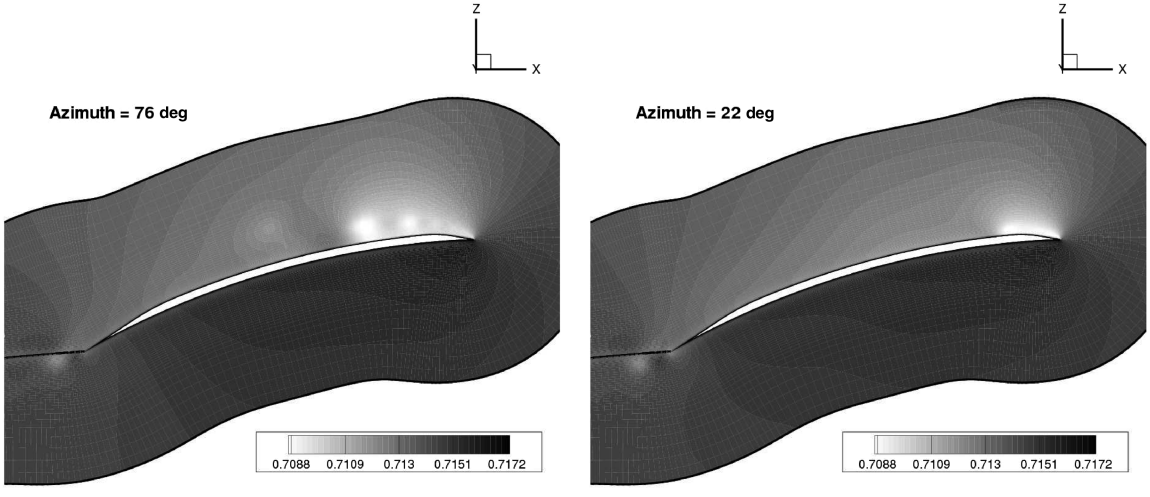

Fig. 14 Spanwise pressure contour at $r/R = 0.9$ for microscale coaxial system.

Clearly, the unsteadiness in the forces of the bottom rotor is smallest for $h/R = 0.446$, indicating that the phasing of the vortex impingement upon the bottom rotor can play a significant role in reducing unsteadiness for the microscale coaxial systems.

Effect of Top-Rotor Wake on Bottom Rotor

To better visualize the effect of top-rotor wake on the bottom rotor, an azimuthal contour of the sectional thrust ($R\frac{dC_T}{dr}$) and its fluctuation from the mean value are, respectively, plotted in Figs. 10 and 11, for the bottom rotors for the rotor spacings $h/R = 0.268$ and $h/R = 0.446$. The figures clearly show the unsteadiness on the bottom rotor as the wake from the top rotor encounters the plane of the bottom rotor. The interacting wake increases the thrust outboard and decreases the thrust inboard. The sectional thrust fluctuation contour plot for the $h/R = 0.268$ spacing looks different compared with that for the $h/R = 0.446$ spacing. The reason for the differences is again explained by the different location of the impingement of the top-rotor vortex on the bottom rotor.

To further understand the effect of the top-rotor vortex impingement on the bottom rotor, blade pressure fluctuation contours of the bottom rotor are plotted at three different instances in time (instance 1, 16° before the impingement of the vortex; instance 2, at the time of impingement of vortex; and instance 3, 16° after the impingement of the vortex) for the rotor spacings $h/R = 0.268$ and $h/R = 0.446$ in Figs. 12 and 13, respectively. In these plots, the leading edge of the blade is towards the middle for both the upper and lower surfaces. At instance 1, strong suction pressure starts to build on the upper surface of the outboard region of the blade for both the cases. On the lower surface, the signature of the inboard vortex sheet impinging on the blade can be seen, which is particularly clear for the $h/R = 0.446$ case. At instance 2, the strong suction on the upper surface of the outboard portion of the blade is getting ready to separate from the leading edge for both cases, which can be seen more clearly in Fig. 14, which shows the sectional pressure contour at an outboard spanwise location of $0.9R$. At the same instance, a vortex has already shed from the lower surface of the inboard portion of the blade with a higher pressure peak wave further downstream (the acoustic wave seen on the surface plots); Fig. 15 shows the sectional pressure contour at an inboard spanwise location of $0.55R$ at instance 2. The suction peak associated with the separated vortex on the lower surface is not very strong on the actual surface. At instance 3, both the cases show a three-dimensional shedding in the outboard section of the blade.

As a summary to this section, the interaction of the top-rotor vortex and inboard sheet with the bottom rotor results in unsteady shedding from the leading-edge region both in the outboard and inboard portions of the blade, a phenomenon not seen for the full-scale coaxial rotor. In the outboard portion of the blade, a highly three-dimensional shedding occurs on the upper surface of the blade, whereas the shedding at the inboard portion of the blade occurs on the lower surface and it is more two-dimensional in nature. The reason for this shedding is the change in local angle of attack due to velocity induced by the tip vortex. In the outboard portion of the bottom-rotor blade, the angle increases as the top-rotor vortex impinges upon it, whereas the angle decreases in the inboard portion. As a first guess, the use of sharp leading edge, which could result in significant movement of stagnation point with small changes in angle of attack,

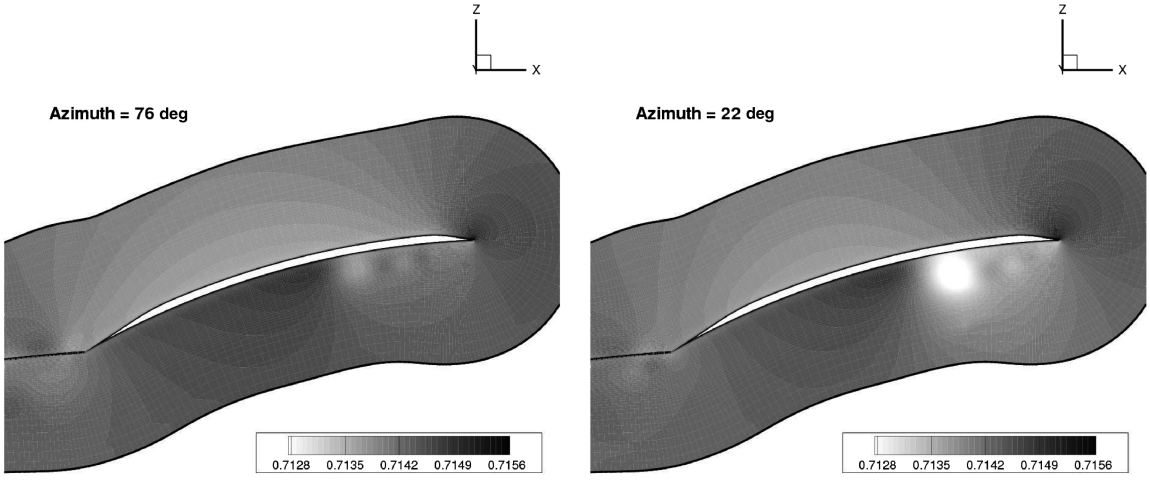

a) $h/R = 0.268$ **b) $h/R = 0.446$**

Fig. 15 Spanwise pressure contour at $r/R = 0.55$ for microscale coaxial system.

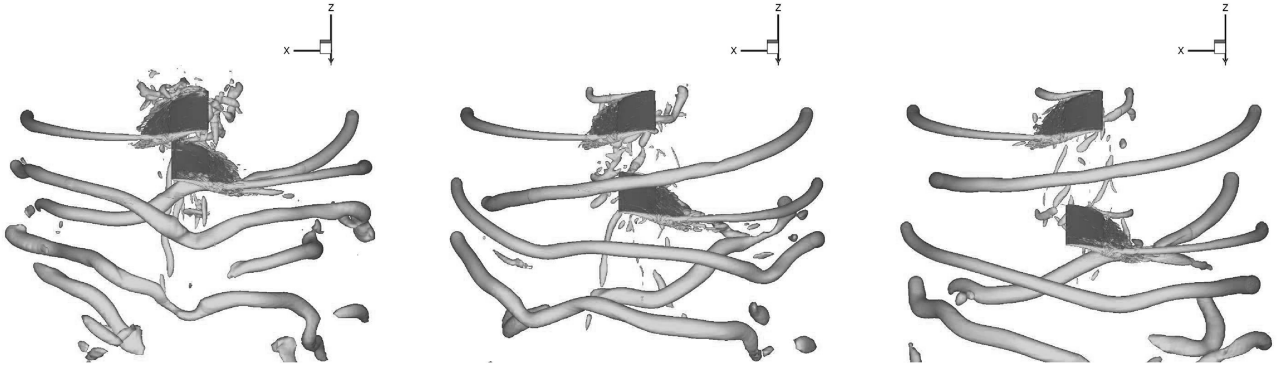

a) $h/R = 0.268$ **b) $h/R = 0.446$** **c) $h/R = 0.625$**

Fig. 16 Isosurfaces of the second invariant of the velocity gradient tensor ($q = 0.2$) for microscale coaxial system when the blades are aligned.

was thought to be the main reason for the drastic unsteadiness. However, further studies revealed that similar unsteadiness is present even when the leading edge of the bottom rotor is rounded. Therefore, the highly unsteady flowfield on the bottom rotor is now believed to arise mainly because of the low-Reynolds-number effects. This fact is supported by the results obtained using a two-dimensional study of the flow over blade sections at conditions found near $0.75R$. At these low Reynolds numbers, the flow is seen to have a high tendency to separate and remains attached only for a very limited range of angles of attack. Therefore, any change in angle of attack caused by the impinging top-rotor wake can lead to significant separation on the bottom rotor.

Wake Trajectory

To extract only the rotational flow regions and not the highly strained regions, the isosurfaces of so-called q-criterion [15] are shown in Fig. 16 for the rotor spacings $h/R = 0.268$, $h/R = 0.446$, and $h/R = 0.625$. These plots are obtained when the top and bottom rotors are aligned with each other. From the figure, it can be seen that the tip vortices are resolved for two blade passages for all the cases. Beyond this wake age, the background mesh becomes too coarse to accurately represent the details of the tip vortex. After passing the bottom rotor, there is a significant interaction between the tip vortices. There is also some evidence of straining in the tip vortex from the preceding bottom-rotor blade as it passes under the subsequent bottom-rotor blade.

Figure 17 shows the wake trajectory at the same instant of time for all three rotor spacings. The radial contraction of the wake of the top and bottom rotors with the azimuth are, respectively, plotted in Figs. 17a and 17b. It can be seen that the wake of the top rotor contracts at a much faster rate compared with that of the bottom rotor for all the cases. This is a result of the interaction between the two wakes, which forces the top-rotor wake inward while pushing the bottom-rotor wake outward. Also, as this interaction occurs at an earlier azimuth for smaller rotor spacings, the amount of contraction of the top-rotor wake is larger at the same azimuth location for smaller rotor-separation distances. For the same reason, the top-rotor wake gets wavy at an earlier azimuth when the rotor separation is smaller. Comparing the contraction of the bottom-rotor wakes of the three rotor spacings, we can see that the contraction rate is slightly larger for the $h/R = 0.268$ case, but it is not too different for the other two rotor-spacing cases. The reason for this could be due to stronger interaction between the wakes for the smallest rotor spacing.

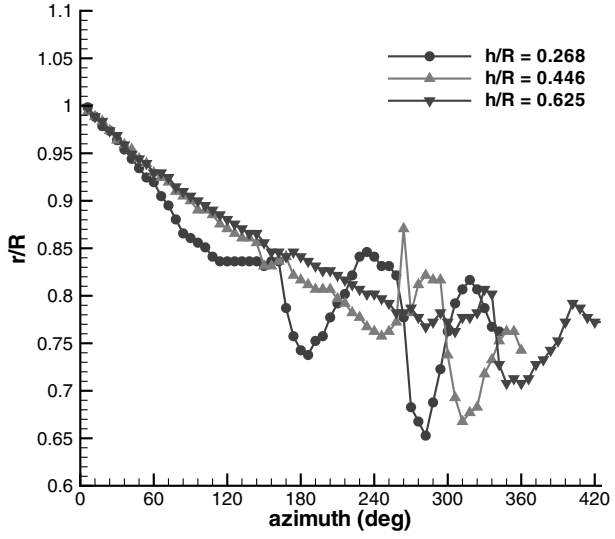

a) r/R vs azimuth (top rotor)

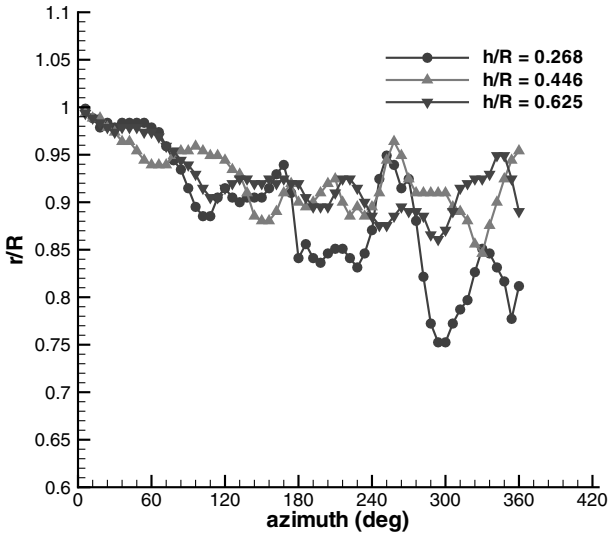

b) r/R vs azimuth (bottom rotor)

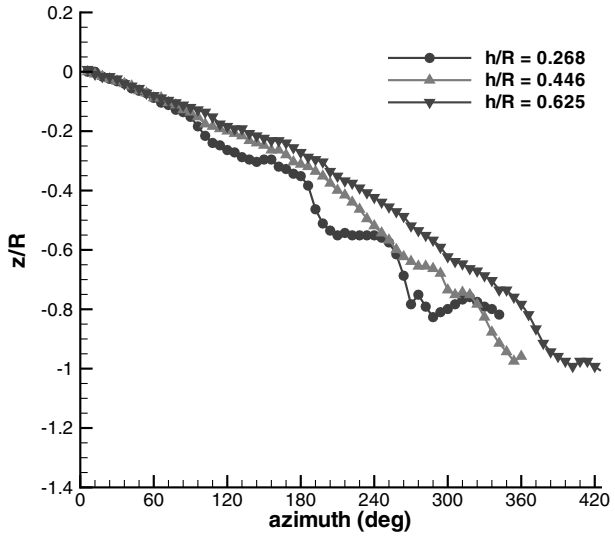

c) z/R vs azimuth (top rotor)

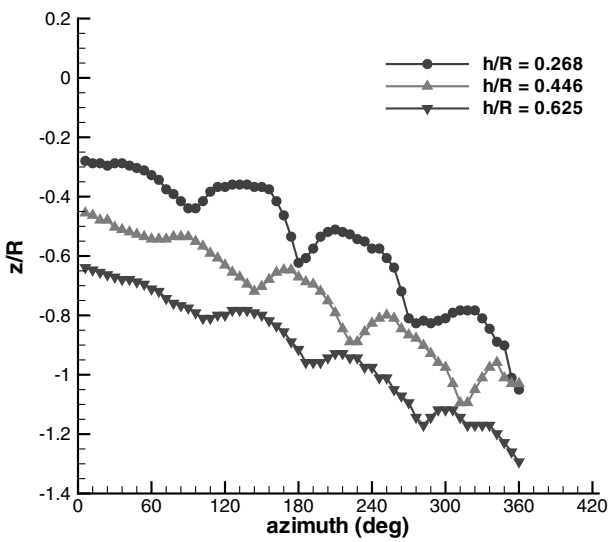

d) z/R vs azimuth (bottom rotor)

Fig. 17 Wake trajectories for various rotor spacing for microscale coaxial system when the blades are aligned.

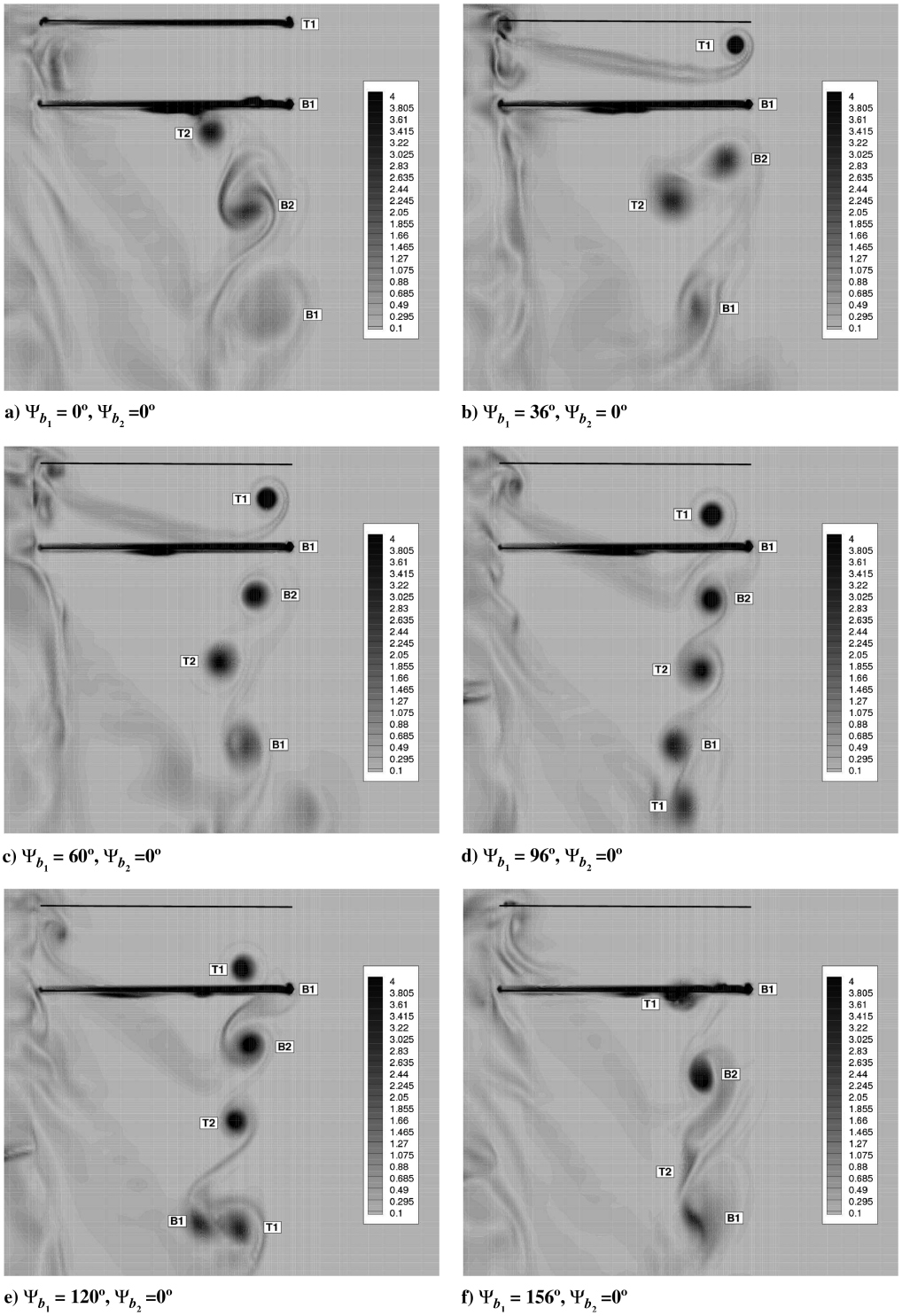

a) $\Psi_{b_1} = 0^o$, $\Psi_{b_2} = 0^o$ b) $\Psi_{b_1} = 36^o$, $\Psi_{b_2} = 0^o$

c) $\Psi_{b_1} = 60^o$, $\Psi_{b_2} = 0^o$ d) $\Psi_{b_1} = 96^o$, $\Psi_{b_2} = 0^o$

e) $\Psi_{b_1} = 120^o$, $\Psi_{b_2} = 0^o$ f) $\Psi_{b_1} = 156^o$, $\Psi_{b_2} = 0^o$

Fig. 18 Vorticity magnitude contours in the plane of the bottom-rotor blade at different instances in time for microscale coaxial system, $h/R = 0.268$.

Figures 17c and 17d respectively show the vertical convection of the top- and bottom-rotor wakes with the azimuth for all three rotor-spacing cases. Clearly, the wakes of the top rotor convect at a faster rate compared with bottom-rotor wakes due to the presence of increased inflow. Both the wakes show increased vertical convection rate after the first blade passage at 180° azimuth. The top-rotor wakes show additional increase in vertical convection rate when they encounter the bottom rotor. As a result, when the rotor spacing is smaller, the vertical convection rate of the top-rotor wake increases at an earlier azimuth, therefore showing larger convection at the same azimuth location compared with a larger rotor-spacing case. The vertical convection rate of the bottom-rotor wake is not too different for all the rotor spacings.

Flowfield Visualization

Figure 18 shows the vorticity magnitude contours for the $h/R = 0.268$ case in a plane that is fixed with respect to the bottom-rotor blade, at different instances in time. At this plane, the wake age of the tip vortices trailed from the bottom rotor remains constant (0, 180, 360°, etc.), while the wake age of those trailed from the top rotor increases. At the first instance, the top- and the bottom-rotor blades are aligned. The vortices from the first top- and bottom-rotor blades are marked T1 and B1, respectively, while the vortices from the second top- and bottom-rotor blades are marked T2 and B2, respectively. The plot clearly shows the interaction of the vortices from the two rotors with each other and also with the inboard sheet. The impingement of the top-rotor vortex upon the bottom rotor can

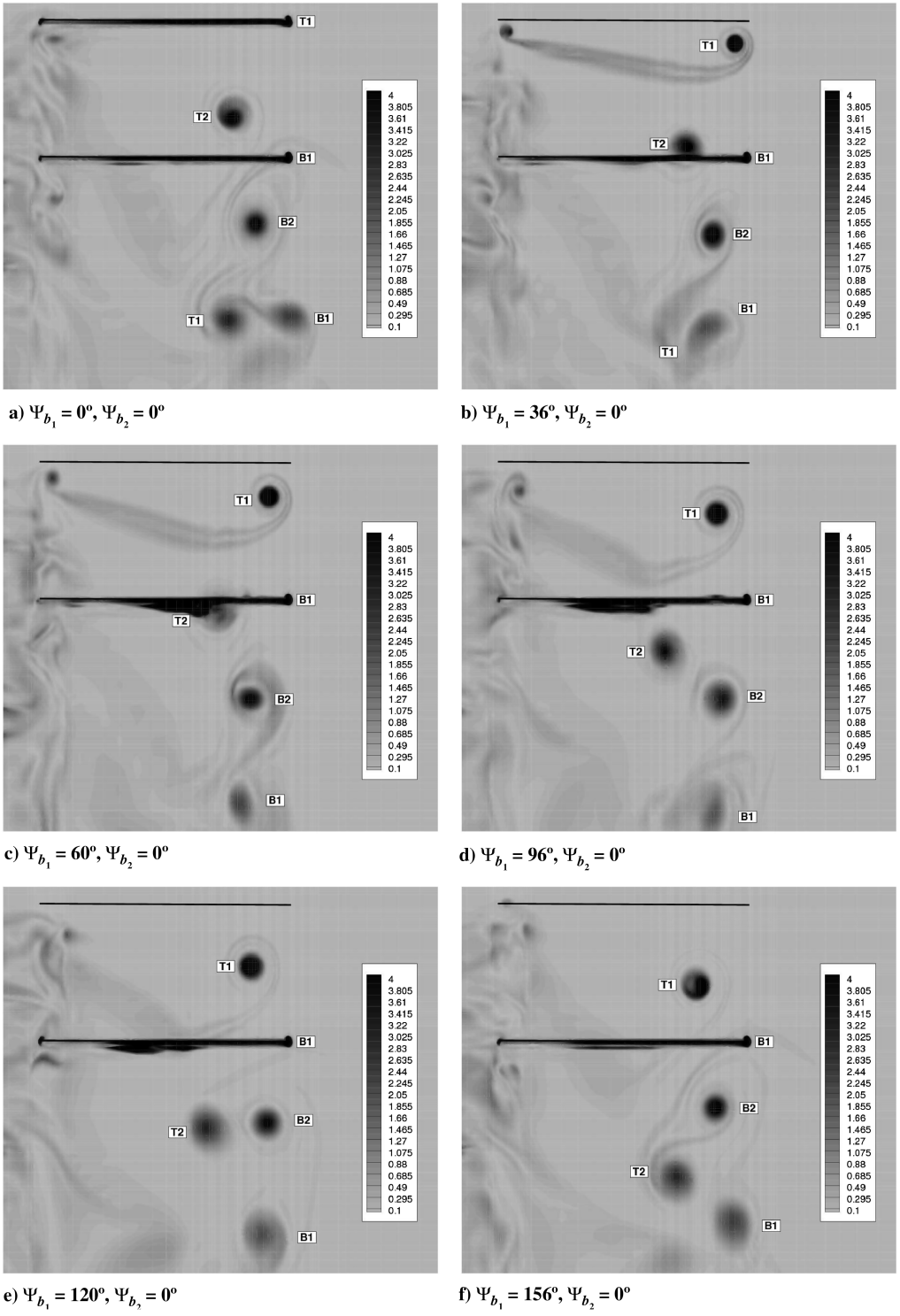

a) $\Psi_{b_1} = 0^o, \Psi_{b_2} = 0^o$ b) $\Psi_{b_1} = 36^o, \Psi_{b_2} = 0^o$

c) $\Psi_{b_1} = 60^o, \Psi_{b_2} = 0^o$ d) $\Psi_{b_1} = 96^o, \Psi_{b_2} = 0^o$

e) $\Psi_{b_1} = 120^o, \Psi_{b_2} = 0^o$ f) $\Psi_{b_1} = 156^o, \Psi_{b_2} = 0^o$

Fig. 19 Vorticity magnitude contours in the plane of the bottom-rotor blade at different instances in time for microscale coaxial system, $h/R = 0.446$.

be seen to have occurred at an instance just before Fig. 18f, which corresponds to 156° wake age of the top-rotor vortex (78° azimuth in time). Recall that, for this rotor spacing, a peak in integrated quantities of the bottom rotor had occurred at about 76° azimuth in time and this plot confirms that the peak is indeed due to the vortex impingement. Similar conclusions can be made for the rotor spacing of $h/R = 0.446$ from Fig. 19. For both cases, we can observe that, even though the vortices trailing from the bottom-rotor vortices are at constant wake age, they are not at a fixed position. Because of the various vortex–vortex and blade–vortex interactions, the tip vortices trailing from the bottom rotor (especially the ones after the first blade passage) show significant wandering. The tip vortices from the two rotor systems are believed to enter into a leap-frogging system, similar to that for vortex smoke rings.

Figure 20 shows the vorticity magnitude contours for $h/R = 0.446$ case in a plane that is at 30° azimuth with respect to the top-rotor blade, at different instances in time. At this plane, the wake age of the tip vortices trailed from the top rotor remains constant (30, 210, 390°, etc.), while the wake age of those trailed from the bottom rotor increases. At the first instance, the top- and the bottom-rotor blades are aligned. At a later time, the bottom-rotor blade can be seen to intersect the plane of interest. Again, significant wandering of the top-rotor tip vortices can be seen due to various interactions, even though they are at a constant wake age.

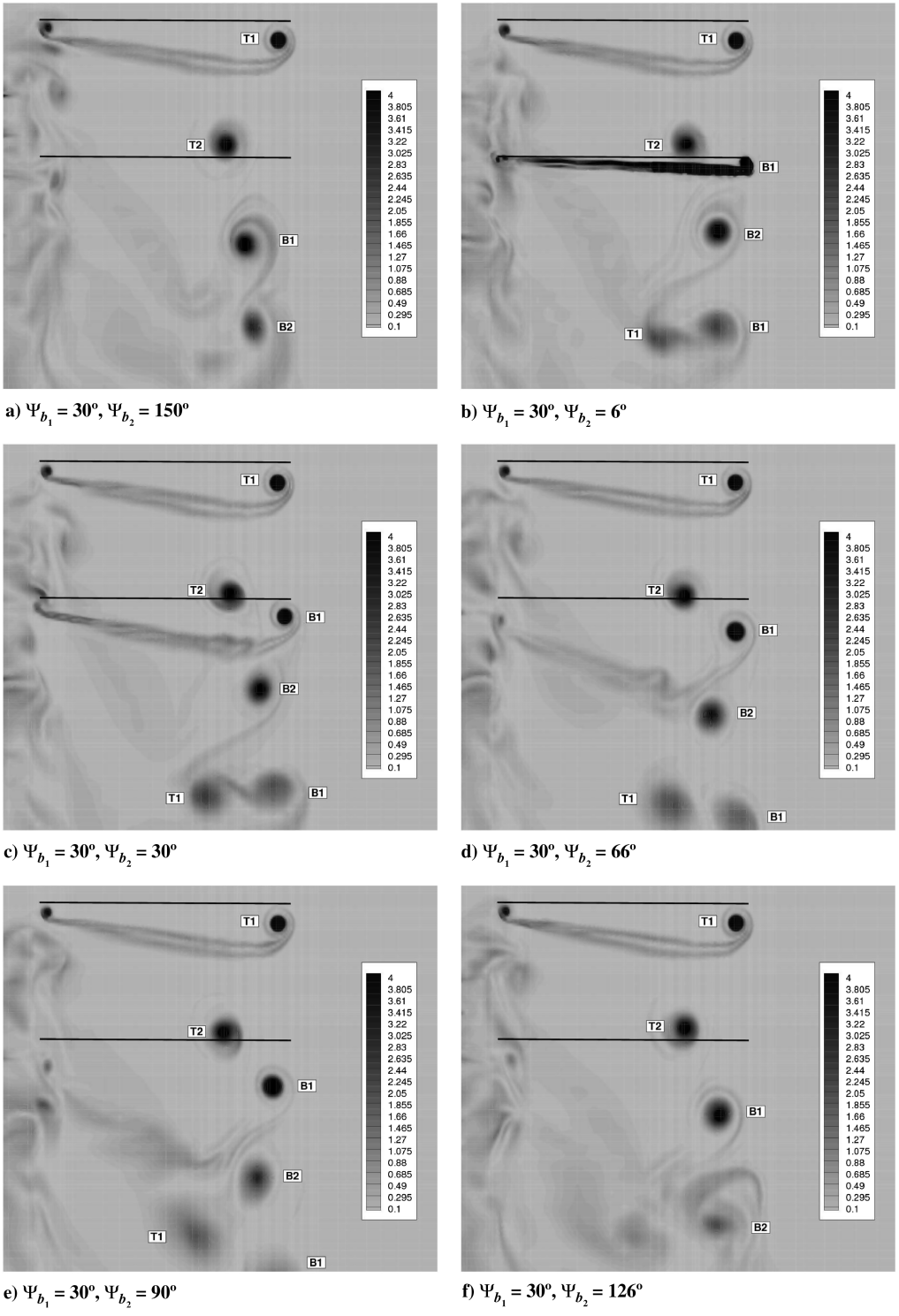

a) $\Psi_{b_1} = 30^o$, $\Psi_{b_2} = 150^o$

b) $\Psi_{b_1} = 30^o$, $\Psi_{b_2} = 6^o$

c) $\Psi_{b_1} = 30^o$, $\Psi_{b_2} = 30^o$

d) $\Psi_{b_1} = 30^o$, $\Psi_{b_2} = 66^o$

e) $\Psi_{b_1} = 30^o$, $\Psi_{b_2} = 90^o$

f) $\Psi_{b_1} = 30^o$, $\Psi_{b_2} = 126^o$

Fig. 20 Vorticity magnitude contours in a plane that is at 30° azimuth from the top-rotor blade at different instances in time for microscale coaxial system, $h/R = 0.446$.

Conclusions

In previous works by the current authors, a compressible Reynolds-averaged Navier–Stokes solver was applied to simulate microscale single rotor and full-scale coaxial rotor. In this paper, a brief summary of some of the previous results were presented.

Performance predictions were very good for all the leading- and trailing-edge geometries for the microscale single rotor. Flow visualization showed that the tip-vortex flowfield is very complicated with the presence of secondary vortices. Additional vortices were found near the trailing edge of the blade over most of the span, a feature which was observed even in the experiments. It was shown in a previous paper [1] by the current authors that the tip-vortex velocity profiles compare reasonably well with the experiments. The peak swirl velocity was predicted reasonably well at all wake ages, whereas the axial deficit along the vortex center and the vortex core radius were overpredicted and the peak vorticity was underpredicted at all wake ages.

The overall performance was predicted reasonably well for the full-scale coaxial system. The bottom rotor showed a degradation of performance due to the influence of the top-rotor wake. Interestingly, even the top rotor showed slight degradation in performance, showing that the bottom rotor has some influence on the top rotor. The top rotor contributes to approximately 55% of the total thrust at all thrust levels. The computed performance data showed that the

flowfield of a coaxial rotor is unsteady with a dominant 4/rev frequency. As a result of the finite thickness of the blade surfaces, the integrated thrust and power showed an impulsive behavior when the blades of the top and bottom rotor were aligned. Additional impulsiveness is generated due to the blade loading. For the bottom rotor, the added influence of the top-rotor wake makes the features more spread-out and distinct.

This was then followed by applying a compressible Reynolds-averaged Navier–Stokes solver to simulate the aerodynamics of microscale coaxial-rotor configuration in hover. The computations were performed on structured body-conforming blade meshes, overset in a cylindrical background mesh. The computations were validated with experimentally measured mean thrust and power and the sources of unsteadiness were examined. The following are specific conclusions that can be drawn from the present work:

1) In the experiment, torque is balanced by changing the bottom-rotor rpm, while keeping the top-rotor rpm fixed. Assuming identical rotational speed for the top and bottom rotors in computation introduces only an error within 5% in the torque balance.

2) The overall performance of the microscale coaxial system is well-predicted for a range of rpm. For the calculations assuming identical rotational speed for the top and bottom rotors, top-rotor thrust is underpredicted by less than $\sim$2% at all speeds, whereas the bottom-rotor thrust is overpredicted by less than $\sim$8%. The total power is also well-predicted.

3) As the rotor spacing increases, the top- and bottom-rotor thrusts show opposite trends. While the top-rotor thrust increases with the rotor spacing, the bottom-rotor thrust decreases as the rotor separation increases. Both the rotor thrusts approach a constant value at very large rotor spacing. The total thrust of the system remains fairly constant with the rotor spacing, which was seen even in the experimental results.

4) Top rotor contributes to about 55% of the total thrust at smaller rotor spacing and increases to about 58% at the largest rotor separation, which is similar to what was seen for full-scale coaxial rotor.

5) The computed performance data showed that the flowfield of a coaxial rotor is unsteady with a dominant $2N$/rev frequency (where N is the number of blades for each rotor). Unsteadiness was mainly caused due to blade loading and wake effect. The unsteady effect due to thickness of the blade (seen in full-scale coaxial rotors) was negligible because of the thin airfoil used. Additional high-frequency unsteadiness was also seen due to shedding near the trailing edge, which was observed even for microscale single rotor.

6) The interactions resulted in a fluctuation of 3–8% in the integrated quantities. Such a fluctuation could be significant for vibration and acoustic characteristics.

7) As the rotor spacing increases, the unsteadiness in the top rotor decreases; however, the unsteadiness in the bottom rotor does not follow any particular trend.

8) For the microscale coaxial system, the wake effect was seen to be comparable or even predominant over the loading effect when the rotor spacing is large. As a result, the phasing of the top vortex impingement upon the bottom rotor can play a significant role in the amount of unsteadiness for the microscale coaxial systems. This is contrary to the full-scale systems, where the loading effect was more predominant over the wake effect, and therefore increase in rotor spacing almost always results in a decrease in unsteadiness of the forces in bottom rotor.

9) The azimuthal contours of sectional thrust and its fluctuation showed unsteadiness on the bottom rotor when the tip vortex from the top rotor impinges upon it. During blade–vortex interaction, the thrust inboard decreased while that outboard increased.

10) Interaction of top-rotor vortex and inboard sheet with the bottom rotor results in unsteady shedding both in the outboard and inboard portions of the blade; a phenomenon not seen for the full-scale coaxial rotor. In the outboard portion of the blade, a highly three-dimensional shedding occurs on the upper surface of the blade, whereas the shedding at the inboard portion of the blade occurs on the lower surface and it is more two-dimensional in nature. The unsteadiness is believed to be mainly caused by the low-Reynolds-number effects.

11) The tip vortices from both the top- and bottom-rotor blades were preserved until two blade passages. Both the tip vortices were clearly identifiable. The interaction of top-rotor vortex with bottom rotor, along with that between tip vortices from the two rotors with each other and the inboard sheet, produces a highly complicated flowfield.

12) The wake of the top rotor contracted at a faster rate compared with that of the bottom rotor because of the vortex–vortex interaction. Additionally, the top-rotor wake convected vertically down at a faster rate due to increased inflow. Interaction between the vortices makes their trajectories wavy.

13) Significant wandering of the tip vortex was observed for both the top and the bottom rotor and it is expected that the tip vortices from the two rotor systems are entering into a leap-frogging system, similar to that for vortex smoke rings.

As a concluding remark, the current work clearly demonstrated the capability of a compressible RANS solver to provide reasonably good prediction of aerodynamic performance and flowfield of a microscale coaxial rotor in hover.

Acknowledgments

This work was supported by the Army's MAST-CTA center on Microsystem Mechanics, Technical Monitor Joseph Mait. The authors wish to acknowledge that the microscale-single-rotor work was funded by the Army Research Office Contract MURI ARMY-W911NF0410176, and the full-scale coaxial work was funded by the National Rotorcraft Technology Center/Center for Rotorcraft Innovation under the "Detailed CFD Simulations of Coaxial Rotor Systems" project (2008-B-11-01.2A9).

References

[1] Lakshminarayan, V. K., and Baeder, J. D., "Computational Investigation of Micro Hovering Rotor Aerodynamics," *Journal of the American Helicopter Society*, Vol. 55, No. 2, April 2010, pp. 022001-1–022001-25. doi:10.4050/JAHS.55.022001

[2] Lakshminarayan, V. K., and Baeder, J. D., "High Resolution Computational Investigation of Trimmed Coaxial Rotor Aerodynamics in Hover," *Journal of the American Helicopter Society*, Vol. 54, No. 4, Oct. 2009, pp. 042008-1–042008-21. doi:10.4050/JAHS.54.042008

[3] Lakshminarayan, V. K., "Computational Investigation of Microscale Coaxial Rotor Aerodynamics in Hover," Ph.D. Dissertation, Department of Aerospace Engineering, Univ. of Maryland, College Park, MD, 2009.

[4] Yoon, S., and Jameson, A., "Lower-Upper Symmetric-Gauss–Seidel Method for the Euler and Navier–Stokes Equations," *AIAA Journal*, Vol. 26, No. 9, Sept. 1988, pp. 1025–1026. doi:10.2514/3.10007

[5] Pulliam, T. H., and Chaussee, D. S., "A Diagonal Form of an Implicit Approximate Factorization Algorithm," *Journal of Computational Physics*, Vol. 39, No. 2, Feb. 1981, pp. 347–363. doi:10.1016/0021-9991(81)90156-X

[6] Buelow, P. E. O., Schwer, D. A., Feng, J., and Merkle, C. L., "A Preconditioned Dual-Time, Diagonalized ADI scheme for Unsteady Computations," *13th AIAA Computational Fluid Dynamics Conference*, Snowmass Village, CO, AIAA Paper 1997-2101, 29 June–2 July 1997.

[7] Pandya, S. A., Venkateswaran, S., and Pulliam, T. H., "Implementation of Preconditioned Dual-Time Procedures in OVERFLOW," *41st AIAA Aerospace Sciences Meeting and Exhibit*, Reno, NV, AIAA Paper 2003-0072, 6–9 Jan. 2003.

[8] Turkel, E., "Preconditioning Techniques in Computational Fluid Dynamics," *Annual Review of Fluid Mechanics*, Vol. 31, Jan. 1999, pp. 385–416. doi:10.1146/annurev.fluid.31.1.385

[9] Spalart, P. R., and Allmaras, S. R., "A One-Equation Turbulence Model for Aerodynamic Flows," *30th AIAA Aerospace Sciences Meeting and Exhibit*, Reno, NV, AIAA Paper 1992-0439, 6–9 Jan. 1992.

[10] Duraisamy, K., "Studies in Tip Vortex Formation, Evolution and Control," Ph.D. Dissertation, Department of Aerospace Engineering, Univ. of Maryland, College Park, MD, 2005.

[11] Srinivasan, G. R., and Baeder, J. D., "TURNS: A Free-Wake Euler/Navier–Stokes Numerical Method for Helicopter Rotors," *AIAA Journal*, Vol. 31, No. 5, May 1993, pp. 959–962. doi:10.2514/3.49036

[12] Lee, Y., "On Overset Grids Connectivity and Automated Vortex Tracking in Rotorcraft CFD," Ph.D. Dissertation, Department of Aerospace Engineering, Univ. of Maryland, College Park, MD, 2008.

[13] Ramasamy, M., Leishman, J. G., and Lee, T. E., "Flow Field of a Rotating Wing Micro Air Vehicle," *Journal of Aircraft*, Vol. 44, No. 4, July 2007, pp. 1236–1244. doi:10.2514/1.26415

[14] Ramasamy, M., Johnson, B., and Leishman, J. G., "Understanding the Aerodynamic Efficiency of a Hovering Microrotor," *Journal of the American Helicopter Society*, Vol. 53, No. 4, Oct. 2008, pp. 412–428. doi:10.4050/JAHS.53.412

[15] Jeong, J., and Hussain, F., "On the Identification of a Vortex," *Journal of Fluid Mechanics*, Vol. 285, 1995, pp. 69–94. doi:10.1017/S0022112095000462

[16] Leishman, J. G., *Principles of Helicopter Aerodynamics*, Cambridge Univ. Press, New York, 2002.

[17] Duraisamy, K., and Baeder, J., "High Resolution Wake Capturing Methodology for Hovering Rotors," *Journal of the American Helicopter Society*, Vol. 52, No. 2, April 2007, pp. 110–122. doi:10.4050/JAHS.52.110

[18] Harrington, R. D., "Full-Scale-Tunnel Investigation of the Static-Thrust Performance of a Coaxial Helicopter Rotor," NACA TN-2318, March 1951.

[19] Huynh, H. T., "Accurate Monotone Cubic Interpolation," *SIAM Journal on Numerical Analysis*, Vol. 30, No. 1, Feb. 1993, pp. 57–100. doi:10.1137/0730004

[20] Leishman, J. G., and Syal, M., "Figure of Merit Definition for Coaxial Rotors," *Journal of the American Helicopter Society*, Vol. 53, No. 3, July 2008, pp. 290–300. doi:10.4050/JAHS.53.290

[21] Nagashima, T., and Nakanishi, K., "Optimum Performance and Wake Geometry of Coaxial Rotor in Hover," *Seventh European Rotorcraft and Powered Lift Aircraft Forum*, Garmisch-Partenkirchen, Germany, Paper 41, 1981.

[22] Syal, M., "Contributions to the Aerodynamic Optimization of a Coaxial Rotor System," Master's Thesis, Department of Aerospace Engineering, Univ. of Maryland, College Park, MD 2008.

[23] Bohorquez, F., "Rotor Hover Performance and System Design of an Efficient Coaxial Rotary Wing Micro Air Vehicle," Ph.D. Dissertation, Department of Aerospace Engineering, Univ. of Maryland, College Park, MD, 2007.